8-2016

Phase field damage simulations of debonding between matrix and spherical inclusions

Johanna B. Palsdottir
Purdue University

Graduate School Form
30 Updated 12/26/2015

PURDUE UNIVERSITY
GRADUATE SCHOOL
Thesis/Dissertation Acceptance

This is to certify that the thesis/dissertation prepared

By Johanna B Palsdottir

Entitled

PHASE FIELD DAMAGE SIMULATIONS OF DEBONDING BETWEEN MATRIX AND SPHERICAL INCLUSIONS

For the degree of Master of Science in Mechanical Engineering

Is approved by the final examining committee:

Marisol Koslowski
Chair

Marcial Gonzalez

Jitesh H. Panchal

To the best of my knowledge and as understood by the student in the Thesis/Dissertation Agreement, Publication Delay, and Certification Disclaimer (Graduate School Form 32), this thesis/dissertation adheres to the provisions of Purdue University's "Policy of Integrity in Research" and the use of copyright material.

Approved by Major Professor(s): Marisol Koslowski

Approved by: Jay P. Gore 7/27/2016

Head of the Departmental Graduate Program Date

PHASE FIELD DAMAGE SIMULATIONS OF DEBONDING BETWEEN MATRIX AND SPHERICAL INCLUSIONS

A Thesis

Submitted to the Faculty

of

Purdue University

by

Johanna B Palsdottir

In Partial Fulfillment of the

Requirements for the Degree

of

Master of Science in Mechanical Engineering

August 2016

Purdue University

West Lafayette, Indiana

To my parents.

ACKNOWLEDGMENTS

I would like to thank my advisor Marisol Koslowski for her supervision in my research and continuous encouragement and guidance throughout my work. I would like to thank Professor Marcial Gonzalez and Professor Jitesh Panchal for participating in my thesis committee. I would also like to show my gratitude to my teammates Yuesong Xie, Bogdan Tanasoiu and Lei Cao and the students who performed the experimental work, Niranjan Parab and Mike Harr, for their help and advice. Additionally, I would like to thank the Fulbright Scholarship Program for my scholarship nomination. It has been a great experience being a Fulbrighter, and I am appreciative of all the opportunities my affiliation has given me. Lastly, I would like to thank my family and friends for always being there for me.

TABLE OF CONTENTS

LIST OF FIGURES

LIST OF TABLES

ABSTRACT

Palsdottir, Johanna M.S.M.E., Purdue University, August 2016. Phase Field Damage Simulations of Debonding between Matrix and Spherical Inclusions. Major Professor: Marisol Koslowski, School of Mechanical Engineering.

Polymer-bonded explosives (PBX) are complicated composites, and it is important for practical applications to know how they deform and fracture. PBX consists of large volume fraction of energetic particles and experiments show that the interface is a critical region for structural stability since particles are often weakly bonded to the polymer and cracks initiate there and the composite fractures. This study focuses on the interface between a particle and a binder and how the particle inclusion starts to debond from the polymer binder in compressive and tensile loading.

A phase field damage model is used to model the response of a glass bead particle in a Sylgard 184 binder under compressive loading, and the model is validated with a Kolsky bar experiment of the same set-up. The comparison between the simulations and the experiment reveals that the damage model should be described with positive volumetric strain only, and deviatoric strain does not contribute to damage in compressive loading of Sylgard 184.

In tensile loading, the phase field damage model is used to study cavitation and debonding, as compared with results from literature. In cavitation the interface is perfectly bonded and the fracture initiates slightly away from the interface. In debonding the interface is weaker than the matrix, and fracture initiates at the interface. Analytic solution of the critical stress needed for debonding shows good agreement with the simulations from the model.

CHAPTER 1. INTRODUCTION

It is important to understand how composite energetic material systems behave in practical applications, such as how they deform and fracture when an external load is applied. Energetic materials are a class of material with a high amount of stored chemical energy that can be released. Explosives would be such an example. Comprehensive knowledge of the material properties and the inter-material relationship for this class of materials is essential and, in particular, the knowledge of the material property that describes the resistance to fracture, i.e. the energy release rate or G_c. According to Griffith's criterion [1], a crack will grow if the surface energy, or the work done in creating new surface area by the breaking of atomic bonds, is larger than the energy release rate of the material. Cracks may initiate anywhere in the composite due to some defects in the material, although they most commonly will initiate at the interface where the materials are weakly bonded, and the energy release rate is the lowest in the composite energetic material. Once initiated, the crack can travel along the interface as it propagates through the material [2]. Therefore, the interface between materials often remains the critical region, limiting the overall performance of the composite and as the critical element for structural stability.

1.1 Scope and Objectives

An explosive material is a reactive substance that contains a great amount of potential energy that can produce an explosion if released suddenly. Explosives are hazardous materials and highly susceptible to accidental explosion. Working with explosives can be dangerous and complicated, not to mention difficult and expensive to secure safe manufacturing, storage and handling of the material. Being able to evaluate the ignition process by estimating the strength of the interface or the energy

release rate with simulations would be very beneficial, less time consuming and less dangerous than traditional experiments [2, 3] with materials such as explosives.

Polymer-bonded explosives (PBX) are of particular interest in this study, but several sources affect the ignition process in explosives, such as: crystalline structure of the material, plasticity, porosity, fracture, friction and grain binder interfacial bonding strength. Therefore, understanding crack initiation and propagation is important in developing predictive models of initiation in PBX's.

Polymer-bonded explosives consist of a large volume fraction of energetic particles in a polymer matrix where the polymer bonds the explosive granules into a solid, stable mass. The polymer matrix has a high density in particle-matrix interfaces, therefore the strength of the interface is of key importance to simulate their response. Experiments have shown that failure in PBX occurs primarily at the polymer binder particle interface at low strain rates [4] although fracture also occurs in larger particles [5,6] or by particle-particle contact [7] at high strain rates. To simulate the response of polymer-bonded explosives, the strength of the interface between a polymeric matrix and a particle can be measured experimentally [8,9] and used to calibrate parameters needed in phase field damage model simulations, as discussed in chapter 2 of this thesis. The simulation is validated with the experiment where the energy release rate, G_c, at the interface is varied to represent different interfacial strength. The best fit of G_c to the experimental data and where debonding is observed is selected. Since literature report different values of G_c for same materials [2, 6, 10, 11] it is necessary to calibrate our simulations with an experiment.

After the phase field damage model has been calibrated with the experiment, two failure processes are compared with the literature of Gent et al. [8]. There, see Figure 1.1, failure is studied in a system consisting of a spherical inclusion in a polymer matrix undergoing deformation. These experiments are used to measure the strength of the interface between the particle and the polymer and show two different failure mechanisms: interfacial debonding and cavitation.

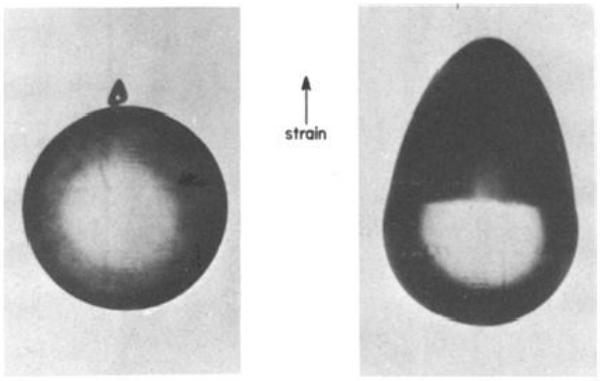

Figure 1.1. Cavitation (left) and debonding (right) in a polymer with a spherical inclusion. Load is applied in the vertical direction [8].

Gent et al. [8] performed several experiments by varying the Young's modulus of the polymer, varying the diameter of the spherical inclusion and by specifying different methods of how the sphere and the binder where chemically bonded. Ultimately the critical stress for cavitation and debonding was found to depend on all of these factors. Results showed that debonding occurs when the matrix-particle interface adhesion is weak and failure originates at the interface while detachment initiates between the two materials. Cavitation, on the other hand, occurs near the interface and it is a failure in the matrix and a small vacuole is formed.

1.2 Thesis Layout

This thesis is divided into four chapters. In chapter 2 the phase field damage model is described and the numerical scheme algorithm which is used to solve the structure fracture problems is explained. Finally, the asymmetric damage response model is explained where damage is driven by volumetric and deviatoric strain.

In chapter 3, numerical simulations with the phase field damage model are validated by comparing to experimental results from a Kolsky bar experiment. The simulations are performed on a glass bead particle sphere inside a Sylgard 184 binder

under compression and tensile loading. Stresses from the simulation are compared to stressed from ABAQUS, and the model is modified to fit the experimental results.

Chapter 4 is a summary identifying the main findings of this research, and the appendix outlines a summary of how to run the phase field damage model simulation.

CHAPTER 2. PHASE FIELD DAMAGE MODEL

2.1 Introduction

Phase field damage model (PFDM) is a model that tracks damage in the material with a scalar variable, the phasefield [12], and is based on Griffith's theory for brittle fracture. Francfort and Marigo [13] introduced the first version of this model in 1998 but Bourdin [12] extended the model to a phase field numerical algorithm and since then many extensions have been made to the model. The model is a variational formulation where the phase field and the structural problem are solved concurrently by the minimization of the total free energy with the constraint of irreversibility to avoid self-healing. Some extensions to the model include: different material responses, loading conditions and dynamic brittle fracture [12, 14–20].

In this chapter the phase field damage model is described in detail. Then, the numerical scheme algorithm used to solve the coupled structure-fracture problems is explained and lastly the asymmetric damage response model is described where damage is driven by volumetric and deviatoric strain.

2.2 Damage Response Model

For a body Ω with a crack area Γ the potential energy of the body is the sum of the elastic energy and the fracture energy. Where the fracture energy is the energy required to create a crack of area Γ for brittle material according to Griffith's criteria [1] and G_c is the energy release rate.

$$W_{pot}(\varepsilon, \Gamma) = W_e(\varepsilon) + W_f(\Gamma) = \int_\Omega a(\varepsilon) dx + \int_\Gamma G_c dx \tag{2.1}$$

In the phase field model approach [21] the fracture energy can be approximated with a volume integral

$$\int_{\Gamma} G_c dx \approx \int_{\Omega} G_c \left[\frac{c^2}{4l_0} + l_0 |\nabla c|^2 \right] dx \tag{2.2}$$

where $c(x) \in [0, 1]$ is the phase field that tracks damage in the material, $c = 1$ where the damage has developed into a crack and $c = 0$ for undamaged material. The model length scale parameter l_0 controls the approximated volume of the damage region. Higher value of l_0 represents a larger width of the crack, see Figure 2.1.

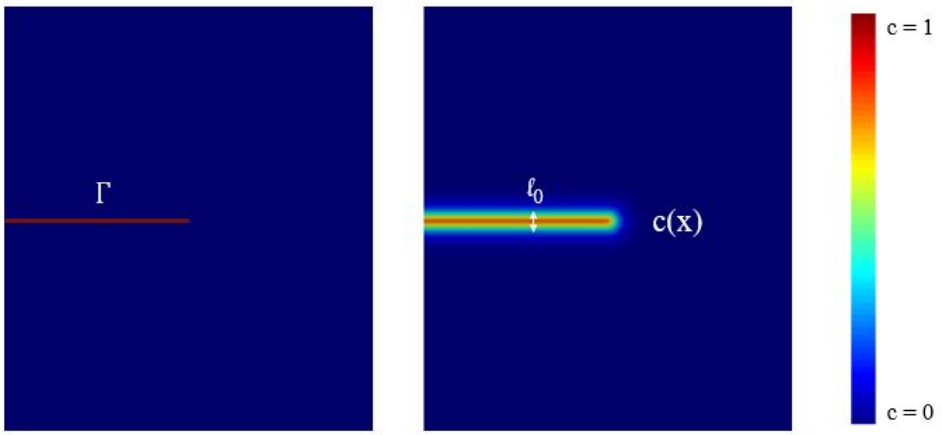

Figure 2.1. (Left) Schematic representation of a solid body with discontinuous crack. (Right) Approximation of the crack with a phase field $c(x)$.

The loss of material stiffness in the failure zone is incorporated into the elastic energy through the phase field with the function $(1 - c)^2$. Experiments have shown that in many materials damage takes place at lower deviatoric stress when materials are under dilatational stress than when they are under compression, so the elastic energy has to be separated into two terms, $W_e^{(-)}$ for compression and $W_e^{(+)}$ for tension.

$$W_e(\varepsilon, c) = W_e^{(+)}(\varepsilon, c) + W_e^{(-)}(\varepsilon) \tag{2.3}$$

Assuming that damage occurs in tension, only the $W_e^{(+)}(\varepsilon, c)$ is affected by damage and it is

$$W_e^{(+)}(\varepsilon, c) = \int_\Omega (1-c)^2 a^+(\varepsilon) dx \tag{2.4}$$

and $W_e^{(-)}(\varepsilon)$ has the form

$$W_e^{(-)}(\varepsilon) = \int_\Omega a^-(\varepsilon) dx \tag{2.5}$$

where $a^+(\varepsilon)$ and $a^-(\varepsilon)$ are strain energy densities. Miehe [15] and Amor [14] proposed different approaches on how the strain energy densities are computed and Amor's approach will be used in this thesis and discussed in section 2.4

The corresponding elastic strain energy rate can be obtained as

$$\dot{W}_e[\varepsilon, \dot{\varepsilon}, c, \dot{c}] = \int_\Omega (\sigma_{ij} : \dot{\varepsilon_{ij}} - 2(1-c)a^+(\varepsilon)\dot{c}) dx \tag{2.6}$$

where the stress is

$$\sigma_{ij} = (1-c)^2 \frac{\partial a^+(\varepsilon)}{\partial \varepsilon_{ij}} + \frac{\partial a^-(\varepsilon)}{\partial \varepsilon_{ij}} \tag{2.7}$$

The fracture energy dissipation due to the increase in damage can be defined as

$$\dot{W}_f(c, \dot{c}) = \int_\Omega G_c \left(\frac{c}{2l_0} + 2l_0 \Delta c \right) \dot{c} dx \tag{2.8}$$

where Δ is the Laplacian. This energy dissipation should be positive because of the irreversibility condition of damage. Therefore the two following conditions need to be satisfied

$$\begin{aligned} \frac{c}{2l_0} + 2l_0 \Delta c \geq 0 \\ \dot{c} \geq 0 \end{aligned} \tag{2.9}$$

To satisfy the local constrains in Equation 2.9, following Miehe et al. [15], an extended Lagrangian is defined [15]

$$L(\varepsilon, \dot{\varepsilon}, c, \dot{c}, \lambda) = \dot{W}_e(\varepsilon, \dot{\varepsilon}, c, \dot{c}) + D(c, \dot{c}, \lambda) \tag{2.10}$$

where the extended dissipation functional $D(c, \dot{c}, \lambda)$ is defined as

$$D(c, \dot{c}, \lambda) = \int_\Omega (2(1-c)a^+(\varepsilon)\dot{c} - \lambda Y_{cr}) dx \geq 0 \tag{2.11}$$

In Equation 2.11, λ is a Kuhn-Tucker coefficient and Y_{cr} is an inequality constrain function defined as

$$Y_{cr} = 2(1-c)a^{+}(\varepsilon) - G_c\left(\frac{c}{2l_0} + 2l_0\Delta c\right) \leq 0 \tag{2.12}$$

The variation of the extended Lagrangian defined in Equation 2.10 with respect to the four variables, results in the following Kuhn-Tucker Equations

$$\begin{aligned} \sigma_{ij,j} &= 0 \\ \dot{c} = \lambda &\geq 0 \\ Y_{cr} &\leq 0 \\ \dot{c} \cdot Y_{cr} &= 0 \end{aligned} \tag{2.13}$$

The first Equation in 2.13 is the equilibrium condition. In the second Equation, the rate of damage is positive, so the damage can only increase, therefore Equation 2.9 is satisfied. The last three Equation in 2.13 together with Equation 2.12 form the governing Equation of the phase field.

$$\left(\frac{4l_0 a^{+}(\varepsilon)}{G_c} + 1\right)(1-c) - 4l_0^2\frac{\partial^2 c}{\partial x_i \partial x_j} = 1 \tag{2.14}$$

The homogeneous form of 2.14 can be calculated by ignoring spatial derivatives of the phase field. Then the solution of Equation 2.14 can be obtained for the damage field as

$$c = \frac{a_0(\varepsilon)}{a_0(\varepsilon) + \frac{G_c}{4l_0}} \tag{2.15}$$

This can be useful when comparing simulations and experiments of homogeneous samples and, as can be easily seen, the damage field approaches to 1 as the elastic strain energy density, $a_0(\varepsilon)$, increases.

2.3 Numerical Algorithm

To optimize the energy with the local minima, an alternative minimization algorithm is used [12,14] but it solves series of minimization of sub problems [20]. At each

step, the displacement u is first solved at a fixed phase field c. Then c is solved at fixed u with the irreversibility condition. This process is repeated until convergence is reached. The solution of displacement and damage can be found as follows:

1. Set $(\mathbf{u}^{(0)}, c^{(0)}) = (\mathbf{u}_{i-1}, c_{i-1})$
2. Set p=1
   - Solve the predictor problem $\mathbf{u}^{(p)}$ with $c = c^{(p-1)}$
   - Solve for $c^{(p)}$ with $\mathbf{u} = \mathbf{u}^{(p)}$ under the constrain $c \geq c_{i-1}$
   - Repeat until $\|c^{(p)} - c^{(p-1)}\| \leq \delta$ or $p = p + 1$
3. Set $(\mathbf{u}_i, c_i) = (\mathbf{u}^{(p)}, c^{(p)})$

A 3D parallel software cells MEMOSA [22] is used which is based on the cell-centered finite-volume method.

2.4 Asymmetric Damage Response Model

Amor et al. [14] proposed a asymmetric damage model where the the strain energy densities are computed from the volumetric and deviatoric strain as follows,

$$\begin{aligned} a^{+}(\varepsilon) &= \frac{1}{2}(\lambda + \frac{2}{3}\mu)\langle\varepsilon^{v}\rangle^{2} + \mu tr[(\varepsilon_{ij}^{dev})^{2}] \\ a^{-}(\varepsilon) &= \frac{1}{2}(\lambda + \frac{2}{3}\mu)(\varepsilon^{v} - \langle\varepsilon^{v}\rangle)^{2} \end{aligned} \tag{2.16}$$

where λ and μ are the Lamé constants and

$$\langle x\rangle = \begin{cases} x & \text{if } x > 0 \\ 0 & \text{if } x \leq 0 \end{cases} \tag{2.17}$$

The deviatoric and volumetric strain are defined as

$$\varepsilon^{d} = \sqrt{\frac{1}{2}[(\varepsilon_1 - \varepsilon_2)^2 + (\varepsilon_1 - \varepsilon_3)^2 + (\varepsilon_2 - \varepsilon_3)^2]} \tag{2.18}$$

$$\varepsilon^{v} = \varepsilon_1 + \varepsilon_2 + \varepsilon_3 \tag{2.19}$$

and the deviatoric and volumetric stress are defined similarly

$$\sigma^d = \sqrt{\frac{1}{2}[(\sigma_{11} - \sigma_{22})^2 + (\sigma_{22} - \sigma_{33})^2 + (\sigma_{33} - \sigma_{11})^2]} \tag{2.20}$$

$$\sigma^v = \frac{\sigma_{11} + \sigma_{22} + \sigma_{33}}{3} \tag{2.21}$$

The strain energy density affected by damage relies therefore on the sign of the local volume change and the material demonstrates asymmetric behavior in tension and compression loading where the compressive part doesn't contribute to damage.

CHAPTER 3. DAMAGE IN A POLYMER MATRIX WITH A SPHERICAL INCLUSION

3.1 Introduction

In this chapter simulations, using the phase field damage model from chapter 2, are validated by comparing to experimental results to gain a better understanding of the strength of the interface between two materials and parameters needed for the phase field damage model. As discussed before, PBX contains a large volume of particles in a binder and therefore it can be difficult to estimate the energy release rate at the interface. To simplify the geometry, experiments are performed with only one particle in a binder so the experiment is better controlled and hence easier to simulate and compare. The simulations are performed on a glass bead particle sphere in a Sylgard 184 binder under compressive and tensile loading. Although these simulations don't involve explosive material, the Sylgard 184 binder is often used as a binder in polymer-bonded explosives, and the glass bead has material properties of similar magnitude as explosives. This is expected to give good estimate of the parameters needed in the phase field damage model for polymer-bonded explosives. Section 3.2 describes the implementation and the result of the experiment where in section 3.3 the simulation set-up is explained and stresses from the simulation are compared to stresses from an analysis of the finite element software ABAQUS. The results show that the model needs to be modified to agree with experimental results of compression loading in Sylgard 184. Section 3.4 and 3.5 describe the simulation and analysis of the result when the model has been changed to a pure positive tensile volumetric damage model and section 3.6 is the same simulation, now in tensile loading.

3.2 Kolsky Bar Experiment with X-ray Phase Contrast Imaging

At Purdue University, the students Niranjan Parab and Michael Harr [23] in Professor Chen's group, studied the dynamic high strain-rate debonding and fracture of a glass bead particle in a Sylgard 184 binder using high speed synchrotron X-ray phase contrast imaging (PCI) synchronized with modified Kolsky bar equipment [24]. The experimental setup is shown in Figure 3.1.

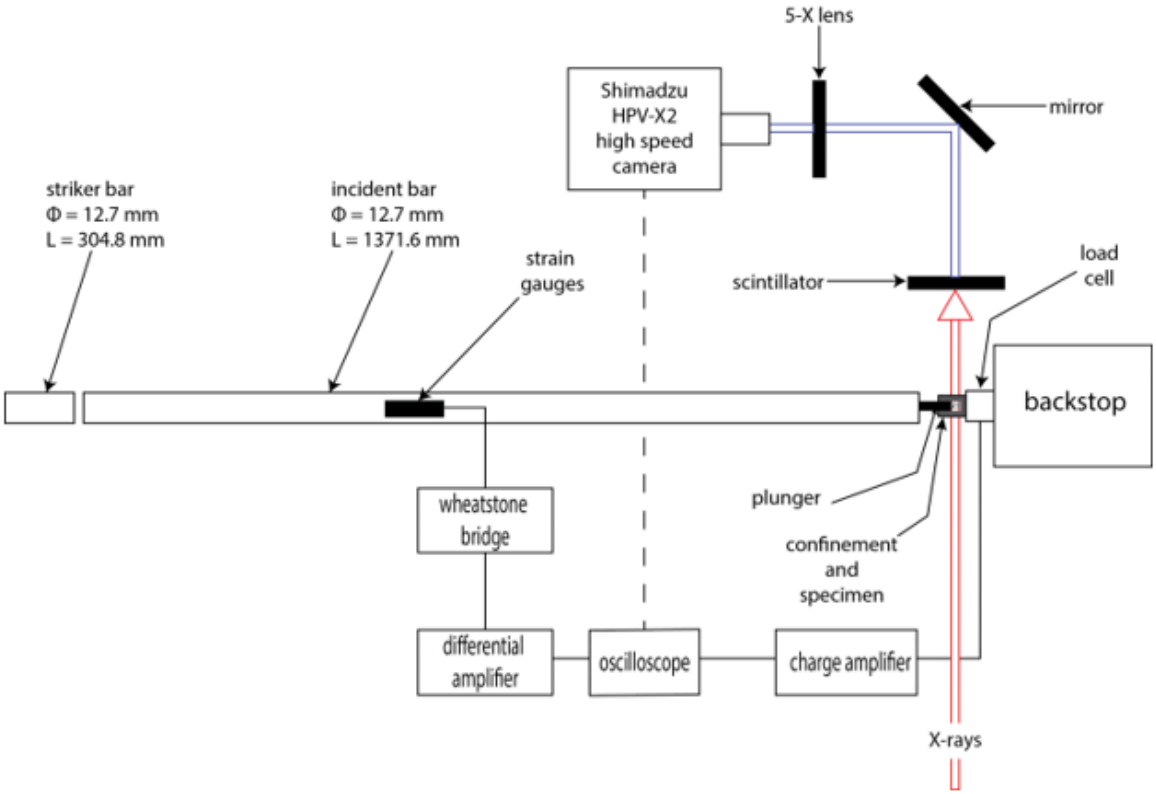

Figure 3.1. Set-up of the Kolsky bar experiment and relative positions of the sample and X-ray beam, picture from Niranjan Parab.

The experiment was performed at the beam line at Argonne National Laboratory using high intensity X-ray PCI measurements. When the X-rays have passed through the sample of the glass bead in the Sylgard binder, X-ray PCI employs the change in

the phase of the X-rays to get high edge resolution pictures which is useful for visualizing cracks and debonding. To convert the X-ray signal to visible light wavelengths, when the X-ray has propagated through the sample, a single crystal scintillator is used. From there it goes through a 45° mirror and a 5-X magnification microscope to the ultra-high speed camera which records the pictures and the resolution was 6.4 $\mu m/px$.

The Kolsky bar set-up is often used to describe material behavior at high strain rates. The modified Kolsky bar used in this experiment, to apply the dynamic compressive loading on the sample, contains a striker bar and an incident bar. Space was limited in the experiment room and therefore the transmission bar in a conventional Kolsky bar set-up was substituted with a load cell fixed on a heavy aluminum backstop. The load cell was used to record the force response of the sample to the incident loading. Strain gauges were attached to the surface of the incident bar to record the incident and the reflected stress waves. The load signals and the strain gauges were synchronized and gathered through an oscilloscope. The recorded load signal was then synchronized with the displacement measurements from the pictures to obtain the force-displacement plot which will be discussed in section 3.3.

The dimensions of the sample can be seen in Figure 3.2 and the glass bead sphere inside the Sylgard 184 matrix has the diameter 676 μm. The sample holder was then placed between the bar end and the load cell, a close up figure of the sample holder can be seen in Figure 3.3. The experiment started with a manual start signal which set off the gas gun and launched the striker bar toward the incident bar and a compressive stress wave was produced in the incident bar as a result of the impact of the striker bar. The strain gauges sensed the stress wave propagating and the strain signal was recorded using the oscilloscope. When the stress wave had propagated through the bar it pushed the plunger onto the sample, where it compressed the sample at a constant velocity of approximately 6 m/s. The high intensity X-ray beam passed through the sample as it was being compressed. The deformation and

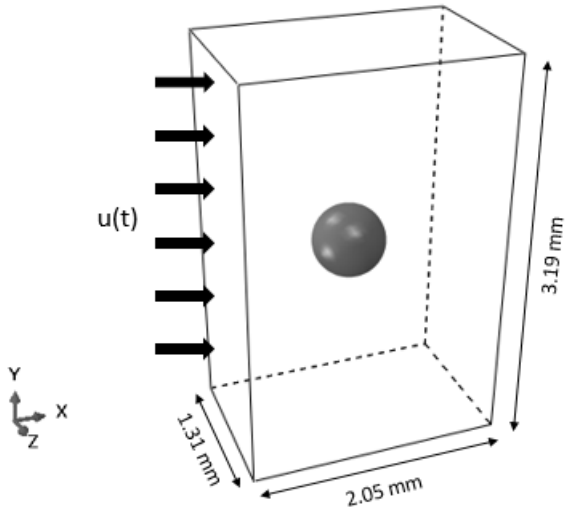

Figure 3.2. Geometry of the sample in the experiment, glass bead sphere in Sylgard 184 binder.

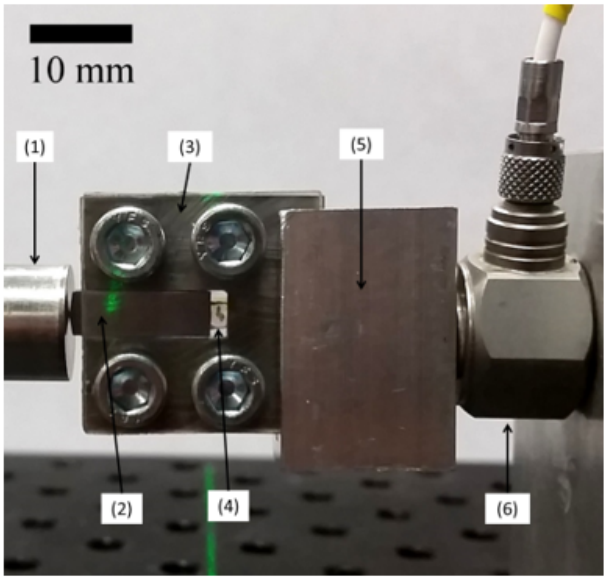

Figure 3.3. Close-up of the sample holder fixed between the bar-end and the load cell, picture from Niranjan Parab. (1) Bar-end, (2) Plunger, (3) PMMA-steel confinement fixture, (4) sample, (5) Fixture to fix the confinement fixture onto the load cell, (6) Load cell.

fracture process in the sample was recorded using the scintillator-camera system as discussed previously.

Figure 3.4 shows frames from the camera at increasing time. The last frame shows how the particle has debonded from the binder on the bottom of the particle. Debonding is expected to initiate at this location because of tension there in the sample but as discussed in the introduction, fracture can initiate anywhere in the material due to defects. To verify that this debonding is not resulting from a defect at the interface, another experiment was later performed with another binder material and debonding initiated at the same location as in Figure 3.4.

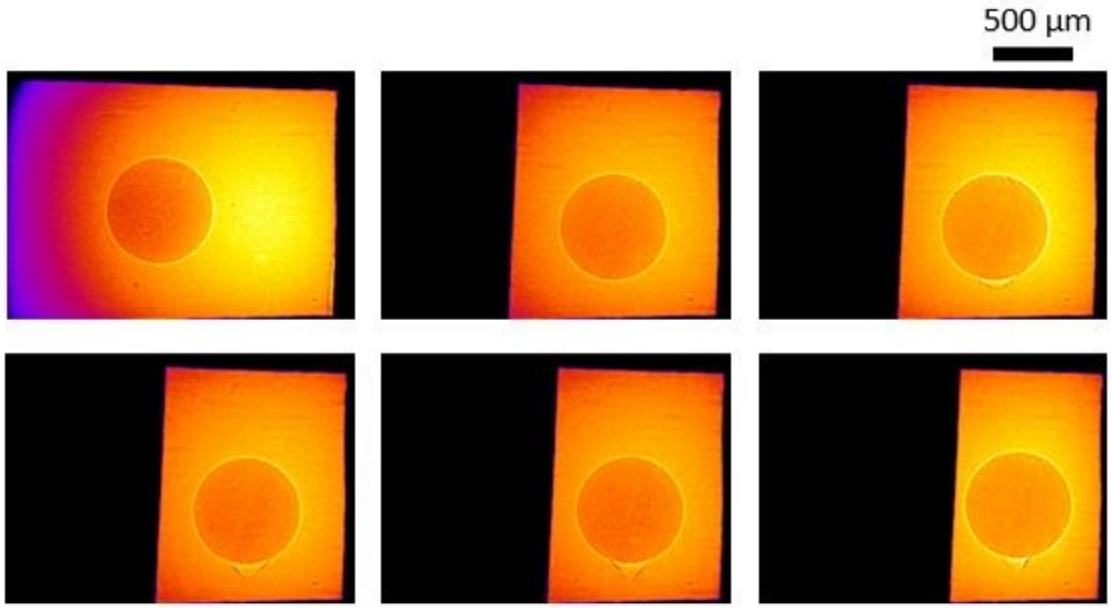

Figure 3.4. Six frames at increasing time of the Kolsky bar experiment of a glass bead particle inside a Sylgard 184 binder where the bar hits the sample horizontally from left. Pictures from Michael Harr [23].

3.3 Simulation Set-Up

Although the experiment is dynamic, the phase field damage model simulations were performed under quasi-static loading for simplicity. Future work involves dynamic simulations with the same set-up which will be a better coherence with the experiment. The simulation has the same geometry as the experiment in section 3.2 but by using symmetry, only one eighth of the domain is simulated and the geometry is rotated, so loading is thus applied on top. The geometry can be seen in Figure 3.5. The right and back boundaries are able to expand freely as in the experiments, all other boundaries are subject to symmetry conditions. The elastic constants and

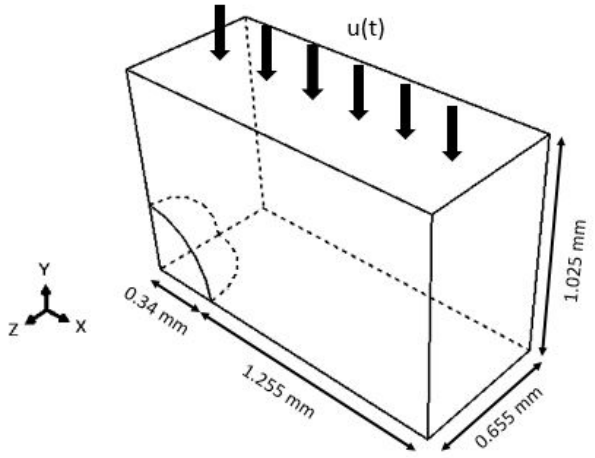

Figure 3.5. Geometry of the sample in the simulation, one eighth of the sample in the experiment, Figure 3.2.

properties used in the simulations are shown in Table 3.1. The elastic constants can be found in literature but G_c and l_0 must be calibrated with experiments. It has been experimentally demonstrated by Johnston et al. [26] that Sylgard 184 has significantly different Young's modulus in tension and compression whereas the compressive modulus is approximately two orders of magnitude larger than the tensile modulus. For example, a Sylgard sample cured at $25°C$, has the tensile modulus as $E = 1.32$

Table 3.1. Material properties used in the simulation.

	Sylgard 184	Glass bead
E	-	70 GPa [25]
ν	0.44 [26]	0.3 [25]
l_0	10 μm	10 μm
G_c	50 J/m^2	400 J/m^2

MPa, while the compressive modulus is $E = 186.9$ MPa. Furthermore, the tensile modulus is observed to increase with curing temperature while the compressive modulus decreases with curing temperature. Therefore simulations with different Young's modulus of the binder were performed and the best fit to the experiment was found. The Poisson's ratio of Sylgard 184 is also not readily available in the literature, with values ranging from 0.44-0.5 [27]. To avoid computational errors because of infinite moduli a value of 0.44 was chosen. The elastic constants of glass bead can be found in Agnolin et at. [25].

The length scale parameter, l_0, is determined to be 10 μm according to the size of the numerical sample to make the simulations feasible. The energy release rate, G_c is difficult to find in literature but for the glass bead it was given a high value such that the particle would not break, since the particle did not break in the experiments. The energy release rate at the interface was given a value of $17 J/m^2$ from Gent et al. [8] which is on the same order of magnitude as many weakly adhered systems [3].

Due to the big difference in the elastic constants from the particle to the matrix, the mesh is refined at the interface and varied exponentially to decrease the large jump in stress across the interface and stress concentrations. The mesh can be seen in Figure 3.6. It has 123,048 linear hexahedral elements and 131,610 nodes. The size of an element is 20 μm but at the interface the size is 2 μm.

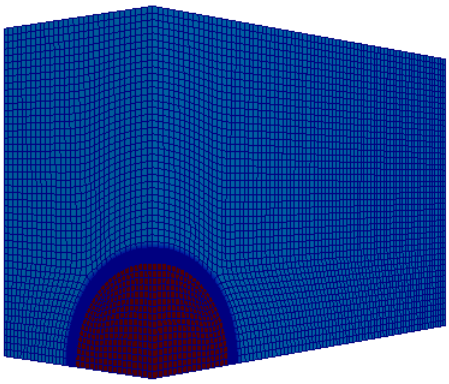

Figure 3.6. Mesh used in the simulation of a spherical inclusion in a polymer matrix, sphere showed in red.

To verify the stress calculations in the model, elastic simulations were compared to the stress output of the finite element software ABAQUS. The stresses in the mesh showed good agreement and less than 3% difference between these two models. One case of comparison of stresses can be seen in Figure 3.7 and 3.8 were the stresses are plotted along a line from the inclusion in the direction of the applied stress, R_0 is radius of the particle.

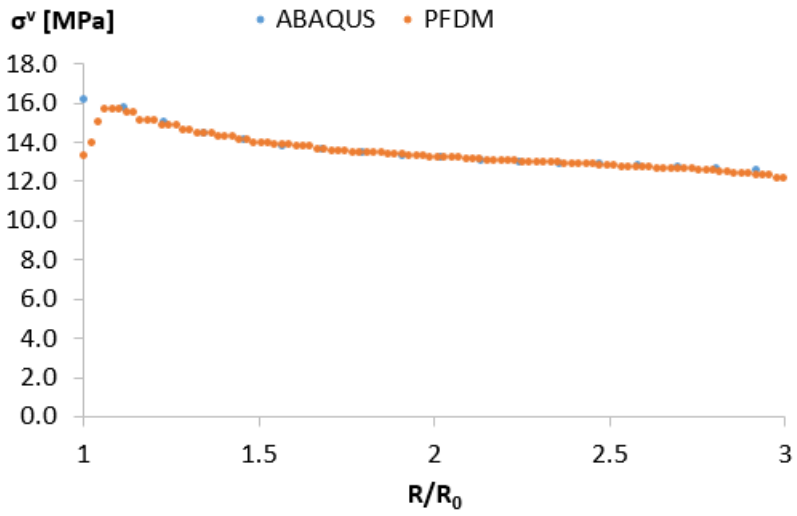

Figure 3.7. Comparison of volumetric stress between PFDM and ABAQUS.

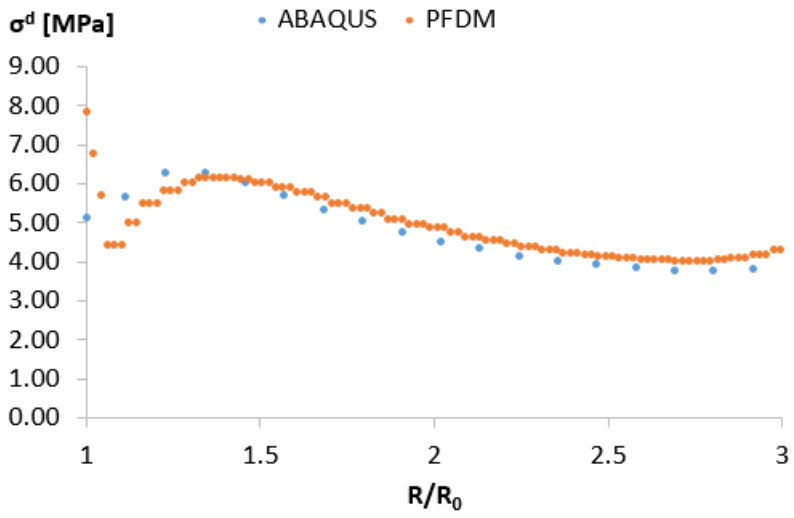

Figure 3.8. Comparison of deviatoric stress between PFDM and ABAQUS.

Simulations were performed with the model described in chapter 2 with the set-up previously discussed. A contour plot of the stress fields, when 375 μm displacement has been applied vertically on top, can be seen in Figure 3.9 and 3.10. The stresses have been normalized with the Young's modulus of the binder. As can be seen in these two figures the highest stress is the deviatoric stress at 45° angle and therefore damage is expected to initiate at this location. Figure 3.11 shows contour plot of the damage field when 375 μm compression loading has been applied vertically on top, were damage is shown in red. As expected, damage initiates at the 45° angle which is not the same location of debonding as was observed in the experiment in Figure 3.4, where the arrow is pointing at in Figure 3.11. It is clear from the location of damage, that the model in chapter 2 does not capture damage well in the positive tensile volumetric part in Sylgard 184 in compressive deformation. The debonding should initiate at the location of tension i.e. at the highest positive volumetric stress, as seen in Figure 3.9. Even though the evolution of the damage field is affected by positive volumetric deformation, the rate of growth is larger for deviatoric stress damage in compression, therefor the model needs to be modified. The force-displacement curve from the simulation was compared to the experimental data. Figure 3.12 shows that

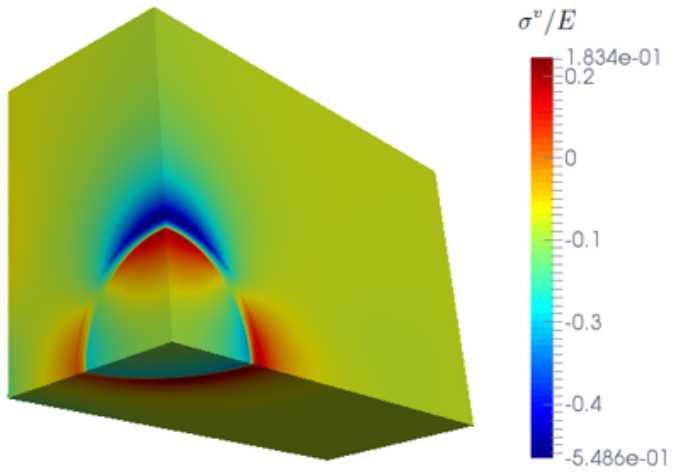

Figure 3.9. Contour plot of the distribution of the volumetric stress normalized with the Young's modulus of the binder when 375 μm has been applied vertically on top. Maximum positive volumetric stress shown in red.

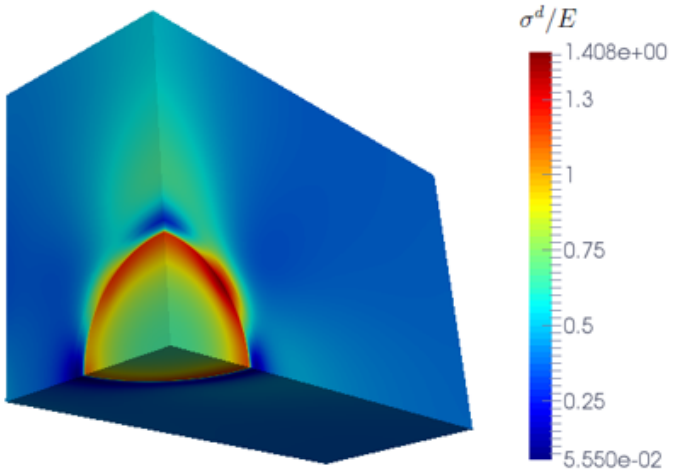

Figure 3.10. Contour plot of the distribution of the deviatoric stress normalized with the Young's modulus of the binder when 375 μm has been applied vertically on top. Maximum deviatoric stress shown in red.

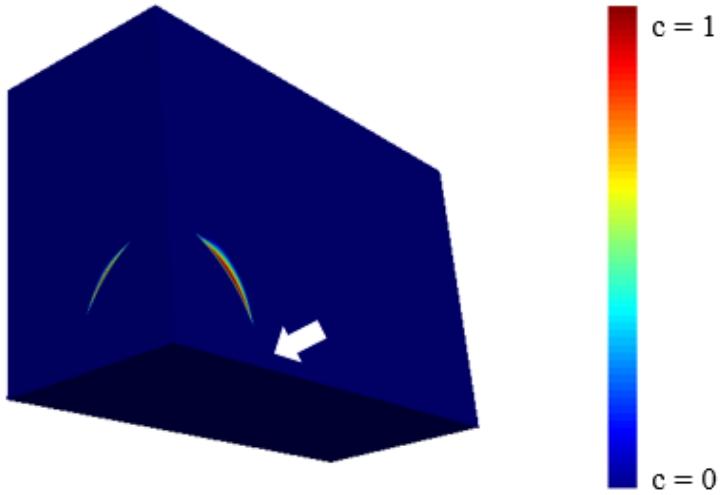

Figure 3.11. Contour plot of the damage field when 375 μm compression loading has been applied vertically on top where the Young's modulus of the binder is 150 MPa, damage is shown in red.

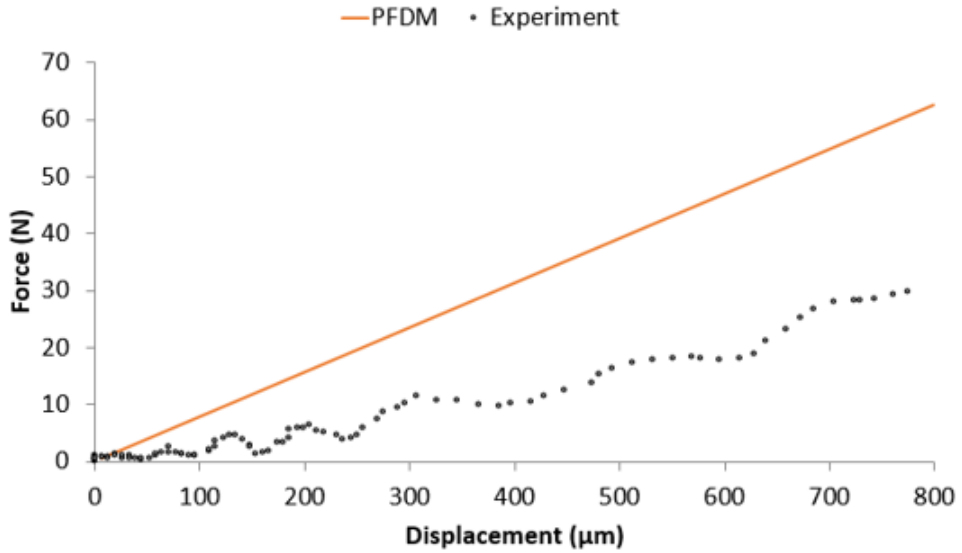

Figure 3.12. Force-displacement curve from the experiment and the PFDM simulations with Young's modulus of the binder as 150 MPa.

the simulation data does not agree with the experimental data and that the binder is too stiff, so the Young's modulus of the binder has to be lower. The curve from the experiment has fluctuation since the experiment is dynamic, but the simulation is quasi-static. After 800 μm, more fluctuations were observed in the experiment but that was due to the continuous move of the plunger after the Kolsky bar stopped since it was not attached.

3.4 Volumetric Damage Model

Due to the disagreement in the damage nucleation with the experiments discussed in previous section, the model needs to be modified for this case where the deviatoric part does not contribute to damage. The strain energy densities in Equation 2.16 are therefore changed to,

$$\begin{aligned} a^+(\varepsilon) &= \frac{1}{2}(\lambda + \frac{2}{3}\mu)\langle\varepsilon^v\rangle^2 \\ a^-(\varepsilon) &= \frac{1}{2}(\lambda + \frac{2}{3}\mu)(\varepsilon^v - \langle\varepsilon^v\rangle)^2 + \mu tr[(\varepsilon_{ij}^{dev})^2] \end{aligned} \tag{3.1}$$

Only $a^+(\varepsilon)$ is affected by damage as was discussed in chapter 2 therefore only the positive volumetric strain is now contributing to damage. The stress can be calculated with Equation 2.16 and 2.7.

$$\sigma_{ij}(\varepsilon, c) = (\lambda + \frac{2}{3}\mu)\langle\varepsilon^v\rangle + 2\mu\varepsilon_{ij}^{dev} + (1-c)^2((\lambda + \frac{2}{3}\mu)\langle\varepsilon^v\rangle) \tag{3.2}$$

3.5 Damage in Compression

Figure 3.13 shows contour plot of the damage field which is based on the pure volumetric damage model discussed in the previous section and Equations 3.1. A 800 μm compression displacement has been applied vertically on top and the Young's modulus of the binder has been lowered to 75 MPa. The specimen is damaging at the maximum positive volumetric stress, at the same location as in the experiment. The particle is also debonding at the bottom of the sample, but since that view of the specimen was not captured by the camera in the experiment it may also have

debonded there. Figure 3.14 shows a better comparison of the experiment and the

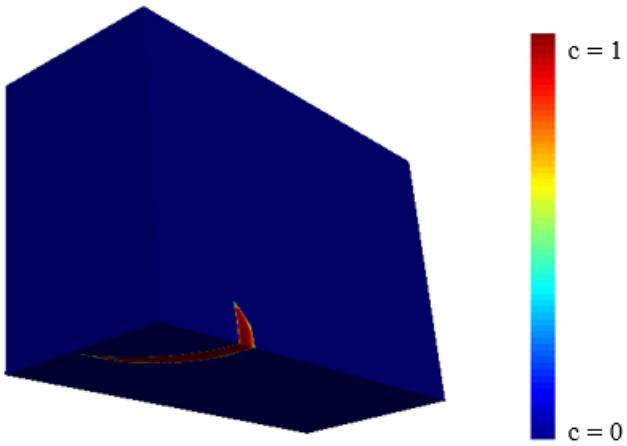

Figure 3.13. Contour plot of the damage field with the volumetric damage model when 800 μm displacement has been applied vertically on top and Young's modulus of the binder is 75 MPa.

simulation, and the same view of the debonding. The color map of the simulation has been changed to better fit to the experiment, and due to the symmetry conditions used, the other half has been added in this figure and the color of the glass bead particle has been made lighter for visibility in comparison.

The force-displacement curve from the experiment and the simulation with Young's modulus of the binder as 75 MPa can be seen in Figure 3.15. These results show better agreement, therefor a Young's modulus of binder as 75 MPa was chosen. It has therefor been shown that the phase field damage model method can be coordinated with experiments to obtain key properties needed for simulations in polymer-bonded explosives.

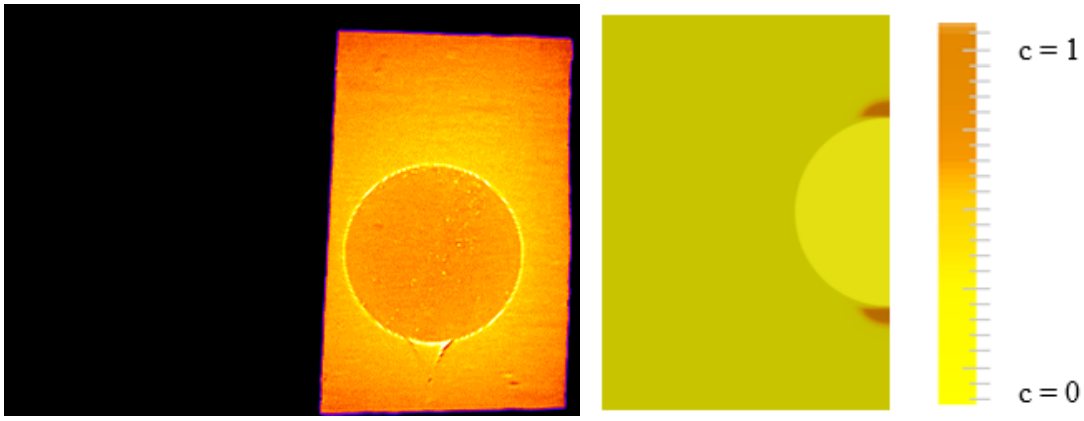

(a) Experiment (b) Simulation

Figure 3.14. Comparison of the debonding in the experiment and the simulation. The sphere in the simulation has been made lighter and the other symmetric half of the sample has been added.

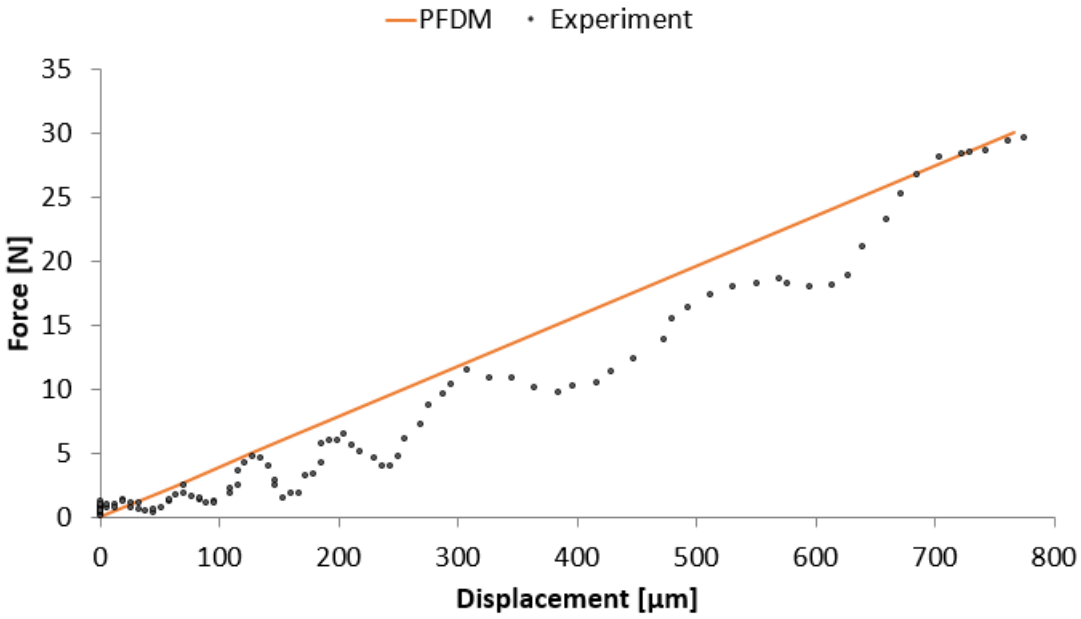

Figure 3.15. Force-displacement curve from the experiment and the PFDM simulations with Young's modulus of the binder as 75 MPa.

3.6 Damage of Spherical Inclusion in Tension

Simulations with the volumetric damage model were also performed with applied tension loading to compare to experiments reported in literature. In particular, the

case of cavitation and debonding were studied and compared with the results from Gent et al. [8] where a glass bead particle in a Sylgard 184 binder, as before, is applied in tension loading. As discussed in the introduction, chapter 1, debonding initiates when the interface is weak, i.e. has lower energy release rate, G_c, at the interface. When the interface is perfectly bonded, cavitation is observed.

Two cases were studied to observe the transition from debonding to cavitation. The same mesh and set-up were used as in section 3.3. For cavitation the energy release rate, G_c, at the interface has the same value as the matrix, 50 J/m^2, making the interface perfectly bonded. In debonding the interface is weaker, setting the G_c at the interface as 17 J/m^2. These two simulations were applied in tensile loading and Figure 3.16 shows the contour plots of the damage when 710 μm tension has been applied vertically on top.

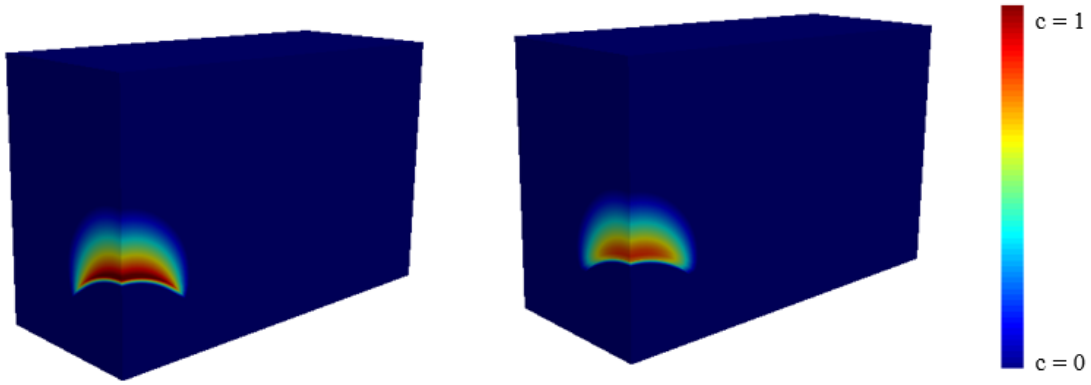

(a) (b)

Figure 3.16. Contour plot for (a) weak interface, $G_c = 17\ J/m^2$ and (b) strong interface, $G_c = 50\ J/m^2$. Damage is shown in red.

The simulation in Figure 3.16(a) with the weak interface shows debonding of the matrix from the particle interface, the damage is right at the interface boundaries. When the interface is perfectly bonded, Figure 3.16(b), damage is observed slightly away from the interface. In this case failure occurs in the matrix, leading to cavitation

as observed in the experiments by Gent et al. [8]. Since the interface is weaker in Figure 3.16(a) more damage has developed.

Gent [28] also derived a theoretical solution of the critical applied stress needed for debonding of a spherical inclusion within an elastic matrix. He considered a small area on the surface of the inclusion and assumed that to be debonded from the matrix initially, see Figure 3.17. The volume ΔV of the debonded region is then given by

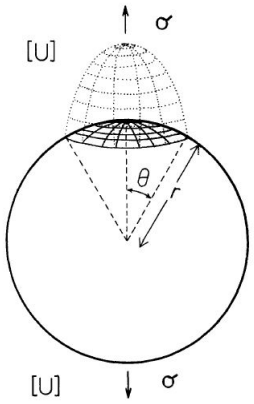

Figure 3.17. Sketch of a single inclusion showing debonded area [28].

$\Delta V = k(rsin\theta)^3$ on general dimensional ground, where $r\theta$ is the radius of the circular debonded zone and k is a dimensionless quantity. The area of the debonded region is $2\pi r^2(1 - cos\theta)$. The loss ΔW in elastic strain energy when the debonded zone increases in area by ΔA is given by

$$\Delta W = U\left(\frac{\partial(\Delta V)}{\partial\theta}\right)\left(\frac{\partial\theta}{\partial A}\right)\Delta A = (3k/4\pi)(Ursin2\theta)\Delta A \tag{3.3}$$

where U is the strain energy density. According to Griffith's fracture criterion [1] as discussed before, the debonded area will grow if the energy required for debonding, i.e. $G_c\Delta A$, where G_c is the energy required to detach the polymer per unit area of interface, is less than ΔW. The criterion for debonding is therefore

$$U \geq \frac{4\pi G_c}{3krsin2\theta} \tag{3.4}$$

Since the relation between the applied stress and strain energy density is $U = T^2/2E$ the applied stress needed for debonding is

$$T = \sqrt{\frac{8\pi E G_c}{3dsin(2\theta)}} \tag{3.5}$$

where d is the diameter of the sphere, k was evaluated as 2, $d = kr = 2r$ and 2θ is the angle where initial debonded circular path nucleates, found to be $10° \pm 5°$ for spherical inclusions [8].

The critical applied tensile stress when debonding was observed was also obtained from the simulations for three different Young's modulus of the matrix. Figure 3.18 shows the applied tensile stress as a function of the Young modulus of the matrix. The

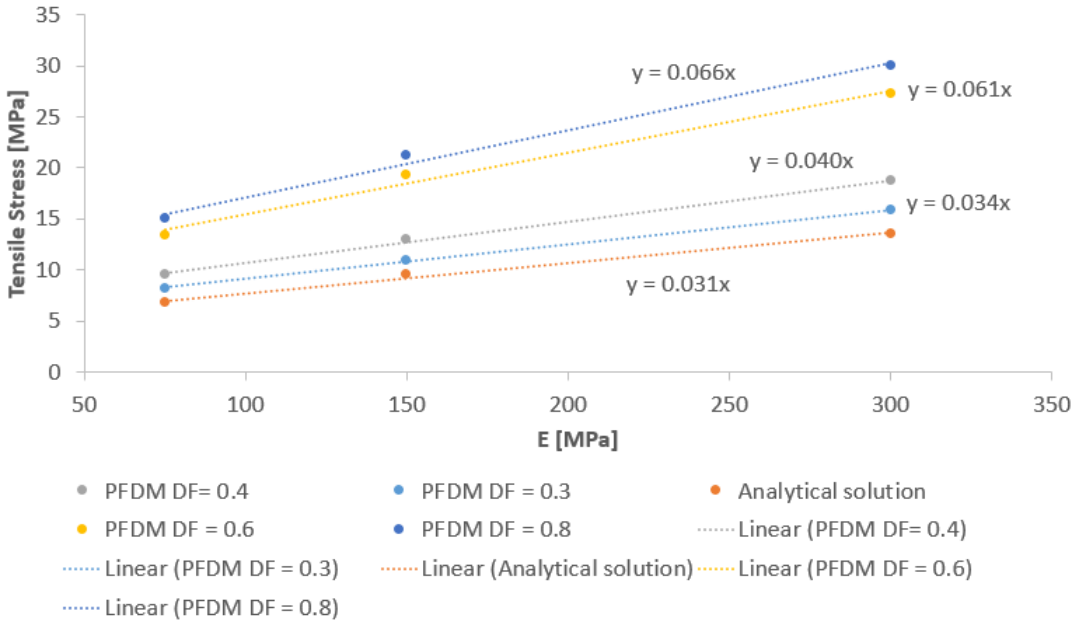

Figure 3.18. Critical debonding tensile stress as a function of the Young's modulus of the matrix. For four different development of the damage fields (DF). DF = 1 equals total fracture.

observation of debonding started when the damage field (DF) had reached a value of 0.4. DF equals 1 is total fracture and DF equals 0 is no fracture. Higher tensile stress is needed to observe more debonding, and it depends linearly on the Young's

modulus of the matrix. When debonding is first observed in the simulation, it shows a agreement with Equation 3.5. These results show that the phase field damage model method gives a good estimate on the tensile stress needed for debonding.

CHAPTER 4. SUMMARY

In this work, polymer-bonded explosives (PBX) are studied to see how they fracture under compressive and tensile loading. Experiments have shown that PBX fracture at the interface between a particle and the binder, and one of the main goals of the research was to simulate the same response in the polymer as was observed in a recent experiment performed by students in Prof. Chen's group at Purdue University.

The experiment was a Kolsky bar experiment where a glass bead particle was inserted inside a Sylgard 184 binder, and it observed how the particle started to debond from the binder. A phase field damage model was used in this research to simulate the experiment with an asymmetric damage response where volumetric and deviatoric strain contributed to damage. The comparison to the experiment was used to obtain important parameters, for example the energy release rate, needed for the phase field damage model in future simulations on PBX.

Comparison showed that the damage response model simulation did not capture the damage in the Sylgard 184 as was observed in the experiment. The deviatoric strain was dominant in comparison to the positive volumetric strain where tension was developing. The damage response model was then modified to a pure volumetric strain damage model and then the improved simulation showed fracture at the same location as in the experiment. A force displacement curve was plotted which was used to calibrate the elastic constants. To verify that the stresses were calculated correctly in the model, an elastic simulation was compared to an analysis by the finite element software ABAQUS. Comparison showed good agreement, or less than 3% difference between the stresses.

Finally, tensile loading was investigated by simulation, where cavitation and debonding were studied and compared to an experiment in literature. Cavitation was observed when the interface was perfectly bonded and fracture initiated at a slight

distance from the interface. When the interface was made weaker than the binder, debonding was observed where fracture initiated right at the interface. An analytic solution of the critical applied stress needed for debonding was reported from literature, and the simulation showed good agreement with that solution. However, more applied stress was needed to see more debonding.

Simulations in this thesis were all based on quasi-static loading for simplicity. However, the Kolsky bar experiment was applied by dynamic loading and therefore it is difficult to compare these two in detail. Dynamic simulation work is in progress and results will be expected soon which will hopefully show a better comparison to the experiment. It will be interesting to determine if the debonding is due to strain or strain rate. More simulations have to be performed to get a better estimate of the energy release rate at the interface since this work only varied the energy release rate from 17-50 J/m^2 at the interface.

LIST OF REFERENCES

LIST OF REFERENCES

[1] Alan A Griffith. The phenomena of rupture and flow in solids. *Philosophical transactions of the royal society of London. Series A, containing papers of a mathematical or physical character*, 221:163–198, 1921.

[2] C Liu, JD Yeager, and KJ Ramos. Bonding energy of sylgard on fused quartz: an experimental investigation. *Philosophical Magazine*, 95(4):346–366, 2015.

[3] AA Volinsky, NR Moody, and WW Gerberich. Interfacial toughness measurements for thin films on substrates. *Acta materialia*, 50(3):441–466, 2002.

[4] PJ Rae, HT Goldrein, SJP Palmer, JE Field, and AL Lewis. Quasi–static studies of the deformation and failure of β–hmx based polymer bonded explosives. In *Proceedings of the Royal Society of London A: Mathematical, Physical and Engineering Sciences*, volume 458, pages 743–762. The Royal Society, 2002.

[5] Zhongbin Zhou, Pengwan Chen, Fenglei Huang, and Siqi Liu. Experimental study on the micromechanical behavior of a pbx simulant using sem and digital image correlation method. *Optics and Lasers in Engineering*, 49(3):366–370, 2011.

[6] SJP Palmer, JE Field, and JM Huntley. Deformation, strengths and strains to failure of polymer bonded explosives. In *Proceedings of the Royal Society of London A: Mathematical, Physical and Engineering Sciences*, volume 440, pages 399–419. The Royal Society, 1993.

[7] JD Yeager, KJ Ramos, S Singh, ME Rutherford, J Majewski, and DE Hooks. Nanoindentation of explosive polymer composites to simulate deformation and failure. *Materials Science and Technology*, 28(9-10):1147–1155, 2012.

[8] A. N. Gent and Byoungkyeu Park. Failure processes in elastomers at or near a rigid spherical inclusion. *Journal of Materials Science*, 19(6):1947–1956, 1984.

[9] TM Mower and AS Argon. An experimental technique to measure the adhesive strength between inclusions and transparent matrices. *Journal of Materials Science*, 93(6):1585–1594, 1996.

[10] John D Yeager, Kyle J Ramos, Daniel E Hooks, Jaroslaw Majewski, and Saurabh Singh. Formulation-derived interface characteristics contributing to failure in plastic-bonded explosive materials. In *15th Int. Detonation Symp*, 2014.

[11] H Tan, C Liu, Y Huang, and PH Geubelle. The cohesive law for the particle/matrix interfaces in high explosives. *Journal of the Mechanics and Physics of Solids*, 53(8):1892–1917, 2005.

[12] Blaise Bourdin, Gilles A Francfort, and Jean-Jacques Marigo. Numerical experiments in revisited brittle fracture. *Journal of the Mechanics and Physics of Solids*, 48(4):797–826, 2000.

[13] Gilles A Francfort and J-J Marigo. Revisiting brittle fracture as an energy minimization problem. *Journal of the Mechanics and Physics of Solids*, 46(8):1319–1342, 1998.

[14] Hanen Amor, Jean-Jacques Marigo, and Corrado Maurini. Regularized formulation of the variational brittle fracture with unilateral contact: Numerical experiments. *Journal of the Mechanics and Physics of Solids*, 57(8):1209–1229, 2009.

[15] Christian Miehe, Martina Hofacker, and Fabian Welschinger. A phase field model for rate-independent crack propagation: Robust algorithmic implementation based on operator splits. *Computer Methods in Applied Mechanics and Engineering*, 199(45):2765–2778, 2010.

[16] JD Clayton and J Knap. A geometrically nonlinear phase field theory of brittle fracture. *International Journal of Fracture*, 189(2):139–148, 2014.

[17] Michael J Borden, Clemens V Verhoosel, Michael A Scott, Thomas JR Hughes, and Chad M Landis. A phase-field description of dynamic brittle fracture. *Computer Methods in Applied Mechanics and Engineering*, 217:77–95, 2012.

[18] MZ Hossain, C-J Hsueh, B Bourdin, and K Bhattacharya. Effective toughness of heterogeneous media. *Journal of the Mechanics and Physics of Solids*, 71:15–32, 2014.

[19] Lisa-Marie Schänzel. Phase field modeling of fracture in rubbery and glassy polymers at finite thermo-viscoelastic deformations. 2015.

[20] Y Xie, Y Mao, L Sun, and M Koslowski. Local versus average field failure criterion in amorphous polymers. *Modeling and Simulations in Materials Science and Engineering*, 23:025004, 2015.

[21] Blaise Bourdin, Gilles A Francfort, and Jean-Jacques Marigo. The variational approach to fracture. *Journal of elasticity*, 91(1-3):5–148, 2008.

[22] Shankhadeep Das, Sanjay R Mathur, and Jayathi Y Murthy. An unstructured finite-volume method for structure–electrostatics interactions in mems. *Numerical Heat Transfer, Part B: Fundamentals*, 60(6):425–451, 2011.

[23] Michael Harr. Afosr progress report 1/21/16. Purdue University. Mehcanical Engineering Building, West Lafayette, IN. 21 January 2016.

[24] Niranjan D Parab, John T Black, Benjamin Claus, Matthew Hudspeth, Jianzhuo Sun, Kamel Fezzaa, and Weinong W Chen. Observation of crack propagation in glass using x-ray phase contrast imaging. *International Journal of Applied Glass Science*, 5(4):363–373, 2014.

[25] I Agnolin and JN Roux. Sound wave velocities in dry and lubricated granular packings: numerical simulations and experiments. *Optical Coherence Tomography in Cardiovascular Research*, page 313, 2007.

[26] ID Johnston, DK McCluskey, CKL Tan, and MC Tracey. Mechanical characterization of bulk sylgard 184 for microfluidics and microengineering. *Journal of Micromechanics and Microengineering*, 24(3):035017, 2014.

[27] Ping Du, I-Kuan Lin, Hongbing Lu, and Xin Zhang. Extension of the beam theory for polymer bio-transducers with low aspect ratios and viscoelastic characteristics. *Journal of Micromechanics and Microengineering*, 20(9):095016, 2010.

[28] AN Gent. Detachment of an elastic matrix from a rigid spherical inclusion. *Journal of Materials Science*, 15(11):2884–2888, 1980.

APPENDICES

APPENDIX A. INITIALIZING THE PHASE FIELD DAMAGE MODEL SIMULATION

The steps used to run the phase field damage model simulation are described in this appendix. The files needed to run a simulation are; a *.cas* file that contains the mesh of the structure, a main *python script* with all the input parameters and the implementation of the phase field damage model. A *.sub* file to submit the simulation to a cluster, which is shown in Appendix B. Two files that write the output files for visualization in the open-source data analysis application Paraview, the visualization of the fracture and the visualization of the stresses and strains. Lastly but most importantly the MEMOSA code with the fracture and structure modules. The input and output scripts are written in Python but the solver is written in C++. The following steps explain the procedure on running a simulation.

- Step 1: Create the mesh of the structure geometry
  (a) The mesh is created in the finite element software ABAQUS. The boundaries of the structure are defined as sets and the mesh must be meshed properly with hexahedral elements to avoid distortion of elements when running the simulation. ABAQUS is used to run the analysis and the mesh is written to an input file, used by Fluent
  (b) The input file from ABAQUS is used in the ANSYS software Fluent. With Fluent the ID's of the boundaries are extracted and the model is scaled to the appropriate scale since ABAQUS does not have a defined metric scale. Finally, the file is saved as a *.cas* file and then it is ready to be used in MEMOSA for the simulation.
- Step 2: The *python script* - the main implementation file of the phase field damage model

(a) Start by initializing the mesh and setting the material properties for the matrix and the particle and tolerance values for the simulation.

(b) Initialize boundary conditions; displacement, stress, symmetry boundary conditions etc.

(c) Define the interface between the particle and the matrix where material properties are varied exponentially.

(d) Decide the loading increment, stress or displacement loading.

- Submit the *.sub* file (Appendix B) to run the simulation on a cluster

  (a) Choose a cluster to run on, the number of nodes and time needed to run the simulation.

  (b) Source to the location of you *env-cluster.sh* file

  (c) Run the simulation

- Visualization when the simulation has run

  (a) The *.vtk* output files produced are used to visualize the results in Paraview

APPENDIX B. SUBMISSION FILE TO A CLUSTER

```
#!/bin/sh -l
# FILENAME:  run_py.sub

#PBS -q marisol
#PBS -l nodes=1:ppn=16
#PBS -l walltime=350:00:00

cd $PBS_O_WORKDIR
source /scratch/carter/j/jpalsdot/FVM_Vol_model/fvm/env-carter.sh

pwd
mpirun -np 16 python ./script.py mesh.cas --type hexa > OutputFile.out
```